https://doi.org/10.5194/wes-2021-84
Preprint. Discussion started: 17 September 2021

WIND ENERGY SCIENCE DISCUSSIONS

Model updating of a wind turbine blade finite element beam model with invertible neural networks

Pablo Noever-Castelos[1], David Melcher[2], and Claudio Balzani[1]

[1]Leibniz University Hannover, Institute for Wind Energy Systems, Appelstr. 9A, Hanover, 30167, Germany
[2]Fraunhofer IWES, Fraunhofer Institute for Wind Energy Systems, Am Seedeich 45, 27572 Bremerhaven, Germany

Correspondence: Pablo Noever-Castelos (research@iwes.uni-hannover.de)

Abstract. Digitalization, especially in the form of a digital twin, is fast becoming a key instrument for the monitoring of a product's life cycle from manufacturing to operation and maintenance, and has recently been applied to wind turbine blades. Here, model updating plays an important role for digital twins, in the form of adjusting the model to best replicate the corresponding real-world counterpart. However, classical updating methods are generally limited to a reduced parameter space due to low computational efficiency. Moreover, these approaches most likely lack a probabilistic evaluation of the result.

The purpose of this paper is to extend a previous feasibility study to a finite element beam model of a full blade, for which the model updating process is conducted through the novel approach with invertible neural networks (INNs). This type of artificial neural network is trained to represent an inversion of the physical model, which in general is complex and non-linear. During the updating process, the inverse model is evaluated based on the target model's modal responses, which then returns the posterior prediction for the input parameters. In advance, a global sensitivity study will reduce the parameter space to a significant subset, on which the updating process will focus.

The finally trained INN excellently predicts the input parameters' posterior distributions of the proposed generic updating problem. Moreover, intrinsic model ambiguities, such as material densities of two closely located laminates, are correctly captured. A robustness analysis with noisy response reveals a few sensitive parameters, though most can still be recovered with equal accuracy. And, finally, after the resimulation analysis with the updated model, the modal response perfectly matches the target values. Thus, we successfully confirmed that INNs offer an extraordinary capability for structural model updating of even more complex and larger models of wind turbine blades.

1 Introduction

Wind turbine blades are enormous composite structures exposed to extreme and harsh environmental conditions. Due to these circumstances, structural health or condition monitoring plays a critical role in reliably ensuring the endurance of the rotor blade. However, this raises the need for an accurate model representation of the structure as built. In this context, the digital twin is emerging as a powerful instrument (Grieves, 2019) for these monitoring systems during operational time, though it can already be involved in early stages of manufacturing (Sayer et al., 2020). The concept of model updating is central to achieving a digital product twin, for example, by updating the preliminary blade design based on sensor responses from blade

https://doi.org/10.5194/wes-2021-84
Preprint. Discussion started: 17 September 2021

characterization tests. This process of model updating ensures that the current stage of the digital twin represents the blade as built.

1.1 Model Updating of Wind Turbine Blades

Model updating has grown in importance in light of digitalization of the wind turbine blades, however, it is only marginally explored in literature. Similar to other structural dynamic model updating applications (Sehgal and Kumar, 2016), the publications on rotor blade model updating typically follow metaheuristic optimization techniques and define the objective function based on the modal assurance criterion (MAC), which represents a common metric for the quantitative comparison of modal shapes (Pastor et al., 2012). Other related modal metrics can be found in Allemang (2003). The most recent publications, such as Hofmeister et al. (2019) and Bruns et al. (2019), apply classical metaheuristic optimization algorithms to update the model parameters and localize damage in a generic problem with a finite element beam blade model. These publications evaluate a global pattern search and compare it to evolutionary, particle swarm, and genetic optimization algorithms. The objective function is based upon the natural frequencies and the MAC value. Furthermore, the MAC and the coordinate modal assurance criterion (COMAC) is applied in the model updating process of a finite element shell model of a rotor blade conducted by Knebusch et al. (2020). That study aims to update the blade model of a built blade along with high-fidelity modal measurements and a gradient-based optimization approach. Another approach presented by Schröder et al. (2018) uses a two-stage metaheuristic optimization to detect damages and ice accretion on a rotor blade. A global optimization with a simulated quenching algorithm is followed by a local method (sequential quadratic programming) to minimize the objective function, consisting of natural frequencies and mode shapes. Omenzetter and Turnbull (2018) implemented metaheuristic optimization methods (fireflies and virus optimization) to detect damages in a finite element beam model of a blade and compare the performance to a simplified beam experiment. Other publications cover simplified model updating procedures of low-level wind turbine blade models (Velazquez and Swartz, 2015; Liu et al., 2012; Lin et al., 2018). While most of the referred contributions focus on the field of damage detection, the model updating conducted by Luczak et al. (2014) highlights the impact of a flexible support structure of the test setup of modern blades, which was also revealed by Knebusch et al. (2020).

1.2 Drawbacks of Current Updating Approaches

The aforementioned approaches can be classified as deterministic and lead to results which are not necessarily the global optima. Therefore, this methodology may require the process to be run several times to ensure the result validity (Schröder et al., 2018; Omenzetter and Turnbull, 2018). This is especially problematic, since metaheuristic optimization algorithms are computationally expensive due to their iterative model evaluation (Chopard and Tomassini, 2018). As a reference, Bruns et al. (2019) performed 500 iterations for two updating parameters and 1,500 iterations for five updating parameters, while in Omenzetter and Turnbull (2018) the firefly optimization of two update parameters required 157 iterations until convergence and the virus optimization 5,000 iterations. Newer model updating techniques involve stochastic approaches such as a sensitivity-based method (Augustyn et al., 2020) or Bayesian optimization (Marwala et al., 2016). The latter is based on sampling techniques such as Markov Chain Monte Carlo to cover the complete parameter space. However, these approaches typically require even

https://doi.org/10.5194/wes-2021-84
Preprint. Discussion started: 17 September 2021

eawe european academy of wind energy
Open Access WIND ENERGY SCIENCE DISCUSSIONS

more model evaluations as stated in Patelli et al. (2017). There, a relatively simple model of a 3 degree-of-freedom mass-spring system demanded 12,000 samples for the Bayesian solution, which was approximately 10 times higher than for the sensitivity-based method.

Most of the aforementioned research encountered three major problems:

1. Due to the aforementioned computational effort, the studies have been restricted to simple models
2. They typically lack an efficient probabilistic approach to evaluate the uncertainty of the results
3. All approaches only address one particular state of the blade at a defined condition and not a generalized inverse model

While in most applications a solution for a particular model is sufficient, an inverted model, which maps model responses to input parameters, can be beneficial, e.g., in quality management during serial production. This reveals a niche for an efficient method to invert the physical model, enabling a fast evaluation of the model states at any time.

1.3 Model Updating via Invertible Neural Networks

This research framework is based on Noever-Castelos et al. (2021a), a feasibility study on a first structural level of wind turbine blades. The research performs a model updating with *conditional invertible neural networks* (cINN) (Ardizzone et al., 2019b) for a cross-section of a wind turbine blade. Noever-Castelos et al. (2021a) considers a reduced number of material and layup parameters as updateable inputs and takes cross-sectional beam properties as model responses to define the objective values. The updating space covers 14 significant input parameters. The specific objective of this current investigation is to extend the feasibility study and methodology in Noever-Castelos et al. (2021a) to a complete finite element beam model of a wind turbine blade, while slightly increasing the input space with additional material properties to update. This investigation is still designed to reveal the feasibility with respect to a more complex model before applying the method to a high dimensional real-world and not generic problem.

1.4 Outline

This study will follow the outline of Noever-Castelos et al. (2021a). The first section after the introduction presents the sensitivity analysis procedure and discusses the physical model built in MoCA (Model Creation and Analysis Tool for Wind Turbine Rotor Blades) (Noever-Castelos et al., 2021b) and BECAS (BEam Cross-section Analysis Software) (Blasques, 2012). The chosen architecture of the cINN is explained in Sect. 3. Section 4 covers the results discussion, with a general analysis of the updating results in Sect. 4.1. Sect. 4.2 reveals intrinsic model ambiguities, before the model robustness to noisy model responses is examined in Sect. 4.3. A resimulationn analysis to ensure the high updating quality is performed in Sect. 4.4. Section 4.5 presents a method to replace the computational expensive sensitivity analysis. This is then all followed by the conclusion in Sect. 5.

https://doi.org/10.5194/wes-2021-84
Preprint. Discussion started: 17 September 2021

2 Sensitivity Analysis of Modal Responses of a Rotor Blade Finite Element Beam Model

Noever-Castelos et al. (2021a) performed a sensitivity analysis to reflect how input distributions influence the output distribution's variance and mean value in order to identify relevant input and output features for the model updating process with the invertible neural network. There, a one-at-a-time approach is used, where values vary individually and their impact on the output is analysed.

2.1 Sobol' Sensitivity Method

In contrast to Noever-Castelos et al. (2021a), this contribution will apply a global variance-based approach, called Sobol method, or Sobol index (Sobol', 1993, 2001). For a multivariate function $y = f(x_1, \dots, x_n)$, Sobol derived, the 1[st] order Sobol index S_i for the variable x_i as follows:

$$S_i = \frac{V\left[\mathbb{E}\left(y|x_i\right)\right]}{V\left(y\right)} \tag{1}$$

This is a measure to what extent the impact of varying x_i will result on the output y. On the basis of a random sampling of the parameters x, $\mathbb{E}(y|x_i)$ represents the expectation E of all y for a constant value of x_i. It can be understood as an average of y corresponding to a slice of the x_i domain in the parameter space. $V\left[\mathbb{E}\left(y|x_i\right)\right]$ is then the variance of all expectations over the range of values of x_i, i.e., slices of the x_i domain (Saltelli et al., 2008). This variance is finally related to the overall variance of y. The 1[st] order Sobol index ranges in $0 \leq S_i \leq 1$. Higher-order Sobol indices can also be extracted, see Saltelli et al. (2008); however, those will be ignored in this work, as we are mainly interested in the influence of individual parameters on the outputs for the feature selection process. For a multivariate function with multiple outputs $(y_1, \dots, y_m) = f(x_1, \dots, x_n)$ Eq. (1) can be expressed as:

$$S_{ij} = \frac{V\left[\mathbb{E}\left(y_j|x_i\right)\right]}{V\left(y_j\right)} \tag{2}$$

2.2 Rotor Blade Finite Element Beam Model

The necessary model generation and variation is performed with the model creator MoCA (Noever-Castelos et al., 2021b) and its interface to BECAS (Blasques and Stolpe, 2012) to create cross-sectional beam properties, which are assembled to a finite element beam (FE beam) and evaluated in ANSYS Mechanical (ANSYS Inc., 2021b). Figure 2 depicts a coarse version of the FE beam used in this study. In contrast to the simplified visualisation, the applied FE beam model is built of 50 3D linear beam elements (BEAM188) (ANSYS Inc., 2021a) with higher mesh density to the root and tip section of the blade, where greater geometrical and material changes are expected. Thus, the finite element model consists of $\dim(N_{\mathrm{FE}}) = 51$ nodes. The input parameter selection of Noever-Castelos et al. (2021a) was slightly expanded to cover more material properties, which will be discussed in detail later. The input parameter selection spans a space with a maximum dimension of $\overline{\mathbb{D}}_{CS} = 33$ for each cross-section, though varying these for each of the 50 cross-sections would result in $\mathbb{D}_{tot} = 1{,}650$ parameters. Assuming a smooth variation of each parameter over the radius, Akima splines (Akima, 1970) were introduced to represent the parameter

https://doi.org/10.5194/wes-2021-84
Preprint. Discussion started: 17 September 2021

variation along the blade. An exemplary spline is depicted in Fig. 1. The spline is built based upon five equidistant nodes, that may vary in y-direction within the given variation range of the parameter.

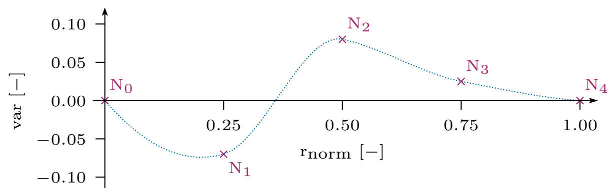

Figure 1. Exemplary variation spline with five nodes.

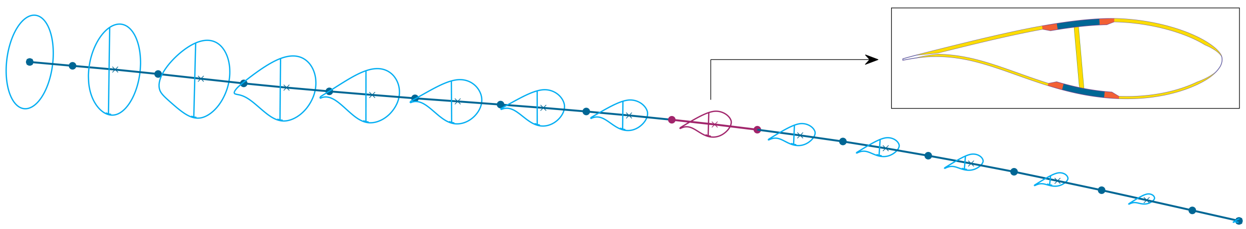

Figure 2. Exemplary finite element beam with reduced number of elements and exemplary cross-sectional illustration. The detail shows a cross-sectional BECAS output (Blasques and Stolpe, 2012) as used in the feasibility study (Noever-Castelos et al., 2021a).

Table 1 summarizes all the investigated input parameters x_i and corresponding properties. Moreover, Table 1 lists the number of spline nodes with their respective normalized radial range and variance limits for each property. In this feasibility study, we consider the most significant independent elastic properties for each material: the density ρ, the Young's modulus E_{11}, the shear modulus G_{12}, and the Poisson's ratio ν_{12}, which may be varied over all five nodes in a range of $\pm$ 10%. Here, we have neglected all thickness-related elastic constants, i.e., parameters including the index/direction 3 and E_{22}, as these parameters offer no significant contribution to the stiffness terms of the beam cross-sectional properties according to Hodges (2006) and Noever-Castelos et al. (2021a). Since foam is modeled as an isotropic material, only two independent elastic properties E, G and the density ρ are considered. In addition to the material properties, the division points are also varied. These subdivide the shell in cross-sectional direction into different sections with a constant material layup or define sub-component positions such as the web or adhesive (Noever-Castelos et al., 2021b). The division point parameters P are allowed to vary on the three mid nodes by the given absolute range. The root and tip node cannot be varied due to model generation issues within MoCA, thus the variance for node N_0 and N_4 will be kept at zero, similar to Fig. 1. All applied variances are approximately twice the permitted manufacturing tolerances (Noever-Castelos et al., 2021a), in order to assure some flexibility of the inverse model. Summing up all parameters and nodes, the problem spans a parameter space of $\dim(x) = 153$. The sensitivity study is conducted based on the Python package *SALib* (Herman and Usher, 2017) and a random sampling dimension of $n = 2^9 = 512$ samples. *SALib* uses the quasi-random sampling with low-discrepancy sequences technique from Saltelli et al. (2008) for the sensitivity analysis. To

https://doi.org/10.5194/wes-2021-84
Preprint. Discussion started: 17 September 2021

compute the Sobol index, the algorithms require a variation of each input feature individually for each of the n samples, which results in a total sample size of $n_{\text{total}} \cdot (\dim(x)+2) = 79,360$ to compute the 1st order Sobol indices. The sensitivity study as well as the updating process is based on the modal beam response y, as described in Gundlach and Govers (2019), in a free-free and a clamped scenario, which is comparable to an elastic suspension of the blade and a fixation of its root to a test rig, respectively. In each case, the first 10 eigenmodes are extracted, excluding the rigid body motion modes in the free-free scenario. For all 10 modes of each modal configuration (free-free and clamped), the natural frequency and the six degrees of freedom of each finite element beam node N_{FE} are saved and summed up to a response dimension of $\dim(y) = (10+10)\cdot(1+6) = 140$. Throughout this paper, input parameters and model responses will also be referred to as input and output features or conditions, respectively.

Table 1. Input feature list analyzed in this study. Each feature and property builds a distribution spline based on the given number of equidistant nodes within the given normalized radial range of the blade. Each node value may then vary in the listed variance range.

Parameter	Property	Nodes	Norm. range	Variance
UD	ρ, E_{11}, G_{12}, ν_{12}	5	[0, 1]	± 10%
Biax45°	ρ, E_{11}, G_{12}, ν_{12}	5	[0, 1]	± 10%
Biax90°	ρ, E_{11}, G_{12}, ν_{12}	5	[0, 1]	± 10%
Triax	ρ, E_{11}, G_{12}, ν_{12}	5	[0, 1]	± 10%
Flange	ρ, E_{11}, G_{12}, ν_{12}	5	[0, 0.1]	± 10%
Balsa	ρ, E_{11}, G_{12}, ν_{12}	5	[0, 1]	± 10%
Foam	ρ, E, G	5	[0, 1]	± 10%
$P_{\text{SS,TE,offset}}$	Location	3	[0.25, 0.75]	± 10 mm
$P_{\text{SS,Mid,spar cap}}$	Location	3	[0.25, 0.75]	± 15 mm
$P_{\text{SS,LE,offset}}$	Location	3	[0.25, 0.75]	± 10 mm
$P_{\text{PS,TE,offset}}$	Location	3	[0.25, 0.75]	± 10 mm
$P_{\text{PS,Mid,spar cap}}$	Location	3	[0.25, 0.75]	± 15 mm
$P_{\text{PS,LE,offset}}$	Location	3	[0.25, 0.75]	± 10 mm

2.3 Feature Selection with Sobol Indicies

After computing the 1st order Sobol index S_{ij} for each input feature x_i and output feature y_i at every N_{FE} position, we obtain a matrix of size 140 x 51 x 153, i.e., $\dim(y)$ x $\dim(N_{\text{FE}})$ x $\dim(x)$. The matrix is then condensed to a single maximum value S_{max} for each input and output feature. Therefore, it is reduced to identify relevant input features y by computing the maximum value along the other non-corresponding dimensions, i.e., dimension 2 and 3. This is done respectively for the output features x along the dimensions 1 and 3. Subsequently, an arbitrary threshold S_{thld} is defined to reject all features with a lower maximum index S_{max}. By this, we aim to consider only features which have a significant impact during at least one event at one location, thus containing enough information for the updating process. Based on experience, we have chosen $S_{\text{thld}} = 0.1$. This leads to the selected features depicted in Table 2 with their corresponding S_{max} and their individual feature index.

https://doi.org/10.5194/wes-2021-84
Preprint. Discussion started: 17 September 2021

When analyzing the rejections, it has to be noted, that all structural properties are condensed to cross-sectional beam properties. That means, for example, Biax 45° as a face layer of the shear web is typically located near the elastic and gravitational center of the cross-sections and thus does not contribute in excess to the mass inertia according to the Steiner theorem, nor to the overall bending stiffness (Gross et al., 2012). Consequently, a variation of ρ_{Biax45} and $E_{11,\mathrm{Biax45}}$ will not significantly impact the modal response of the beam model. However, its shear modulus $G_{12,\mathrm{Biax45}}$ does have an impact when dealing with the shear forces from flap-wise loading. Regarding foam and balsa as sandwich core materials, the stiffness contribution to the sandwich panels is approximately 1% compared to the GFRP (glass fiber-reinforced plastic) face sheets and this makes their variations neglectable, while the mass contributions depending on the layup can reach up to $66-100\%$, which is why a few of the density spline nodes are kept. Summarizing the sensitivity analysis reduced the input feature space to $\dim(x_{\mathrm{sel}}) = 45$, approximately 30% of $\dim(x)$. The output features were all kept according to the feature selection approach. However, a reduced set of radial positions can be applicable as the intrinsic information might be repeated in neighboring N_{FE}, which does not necessarily improve the updating performance, but reduce the performance. Therefore, the output of each third node is selected, ending up with a radial output dimension of $\dim(N_{\mathrm{FE,sel}}) = 17$. Thus, the final dimension for the model updating process of the input feature space is $\dim(input) = \dim(x_{\mathrm{sel}}) = 45$ and of the output feature space is $\dim(output) = \dim(N_{\mathrm{FE,sel}})$ x $\dim(y) = 17$ x 140.

Table 2. Selected feature list from sensitivity study with their respective feature index and maximum 1st order Sobol indicies S_{max}.

Feat.	Parameter	S_{max}	feat.	Parameter	S_{max}
1	$\rho_{\text{UD,N1}}$	0.248	24	$E_{11,\text{Triax,N2}}$	0.485
2	$\rho_{\text{UD,N2}}$	0.382	25	$E_{11,\text{Triax,N3}}$	0.352
3	$\rho_{\text{UD,N3}}$	0.279	26	$E_{11,\text{Triax,N4}}$	0.527
4	$E_{11,\text{UD,N0}}$	0.110	27	$G_{12,\text{Triax,N0}}$	0.371
5	$E_{11,\text{UD,N1}}$	0.435	28	$G_{12,\text{Triax,N1}}$	0.608
6	$E_{11,\text{UD,N2}}$	0.432	29	$G_{12,\text{Triax,N2}}$	0.522
7	$E_{11,\text{UD,N3}}$	0.371	30	$G_{12,\text{Triax,N3}}$	0.594
8	$G_{12,\text{Biax45,N1}}$	0.224	31	$G_{12,\text{Triax,N4}}$	0.343
9	$G_{12,\text{Biax45,N2}}$	0.263	32	$\rho_{\text{Flange,N0}}$	0.214
10	$G_{12,\text{Biax45,N3}}$	0.149	33	$\rho_{\text{Flange,N1}}$	0.620
11	$\rho_{\text{Biax90,N3}}$	0.241	34	$E_{11,\text{Flange,N1}}$	0.414
12	$\rho_{\text{Biax90,N4}}$	0.109	35	$E_{11,\text{Flange,N2}}$	0.486
13	$E_{11,\text{Biax90,N0}}$	0.116	36	$G_{12,\text{Flange,N1}}$	0.332
14	$E_{11,\text{Biax90,N1}}$	0.143	37	$G_{12,\text{Flange,N2}}$	0.276
15	$E_{11,\text{Biax90,N2}}$	0.132	38	$\rho_{\text{Balsa,N1}}$	0.207
16	$E_{11,\text{Biax90,N3}}$	0.219	39	$\rho_{\text{Foam,N2}}$	0.163
17	$G_{12,\text{Biax90,N3}}$	0.112	40	$P_{\text{SS,Mid,spar cap,N1}}$	0.670
18	$\rho_{\text{Triax,N1}}$	0.292	41	$P_{\text{SS,Mid,spar cap,N2}}$	0.433
19	$\rho_{\text{Triax,N2}}$	0.211	42	$P_{\text{SS,Mid,spar cap,N3}}$	0.458
20	$\rho_{\text{Triax,N3}}$	0.463	43	$P_{\text{PS,Mid,spar cap,N1}}$	0.492
21	$\rho_{\text{Triax,N4}}$	0.804	44	$P_{\text{PS,Mid,spar cap,N2}}$	0.550
22	$E_{11,\text{Triax,N0}}$	0.312	45	$P_{\text{PS,Mid,spar cap,N3}}$	0.434
23	$E_{11,\text{Triax,N1}}$	0.375			

3 Invertible Neural Network Architecture

Before proceeding to the model updating process, it is necessary to define the *invertible neural network architecture*. Similar to Noever-Castelos et al. (2021a), this work will built on *conditional invertible neural networks* (cINN) (Ardizzone et al., 2019b) implemented in FrEIA – Framework for Easily Invertible Architectures (Visual Learning Lab Heidelberg, 2021). A basic cINN consists of a sequence of *conditional coupling blocks* (CC), as shown in Fig. 3. Each of these represents affine transformations, that can easily be inverted. The embedded *sub-networks* s_1, t_1, s_2, t_2 embody the trainable functions of this type of artificial neural network.

These *sub-networks* stack the conditions c and the input slice u_2 or v_1 and transforms them for further processing. The stacking necessarily requires similar spacial dimensions of c and u_2 or v_1, respectively. For a further brief introduction to cINN

https://doi.org/10.5194/wes-2021-84
Preprint. Discussion started: 17 September 2021

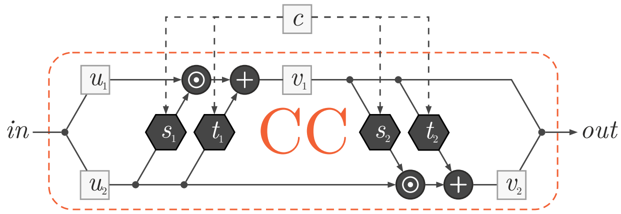

Figure 3. The *conditional coupling blocks* CC with its embedded *sub-network* s_1, t_1, s_2, t_2. This CC architecture can easily be inverted. Ardizzone et al. (2019b)

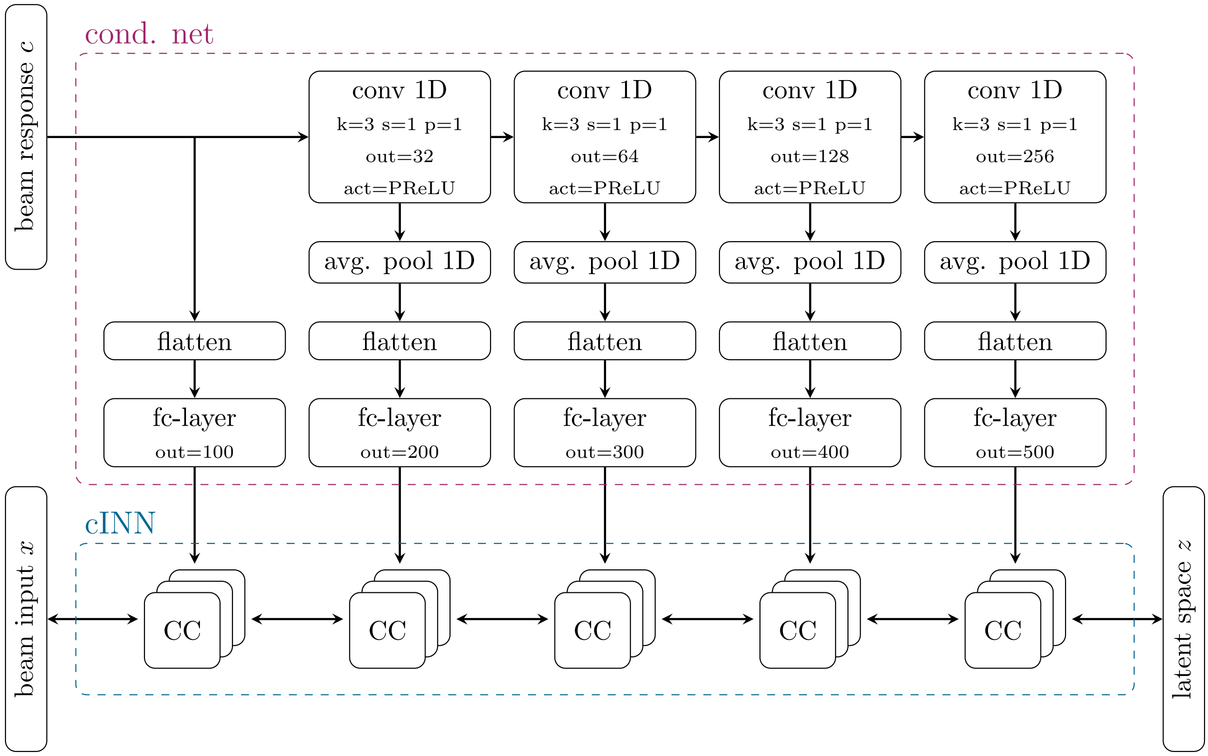

Figure 4. *Conditional invertible neural networks* (cINN, in blue frame) with sequentially connected *conditional coupling blocks* CC. The conditional feed-forward network (cond. net, in violet frame) preprocesses the condition y with 1D convolutional layers and PReLU (parametric rectified linear unit) activations. Average 1D pooling is performed on the output, before it is flattened and reduced in dimension with a fully connected layer (fc-layer), to be then fed into the *sub-networks* of the CCs. The convolutions gradually increases in size in order to progressively extract higher-level features from the condition c.

with topic-related application, please refer to Noever-Castelos et al. (2021a). A more in-depth explanation can also be found in Ardizzone et al. (2019b) and Ardizzone et al. (2018).

https://doi.org/10.5194/wes-2021-84
Preprint. Discussion started: 17 September 2021

Wind Energy Science Discussions

After an extensive hyperparameter study, the presented investigation applies the network depicted in Fig. 4. Hyperparameters describe the network or architecture parameters of artificial neural networks, like number of layers or perceptrons. It consists of a cINN (blue) with a sequence of 15 CCs, grouped into clusters of three. This cINN transforms between the beam input x and the latent space z. However, unlike the underlying feasibility study Noever-Castelos et al. (2021a), an additional feedforward network is implemented, referred to as a *conditional network* (violet). The idea is to preprocess the raw conditions c, i.e., beam responses, before passing them to the *sub-networks* in the CCs. It is trained in conjunction with the cINN, to extract relevant feature information optimally for each stage. The *conditional network* architecture is inspired by Ardizzone et al. (2019b) and should extract higher-level features of c to feed into the sequential CCs, which, according to Ardizzone et al. (2019b), should relieve the sub-networks from having to relearn these higher-level features each time again. With a conditional beam response c of shape $\dim(c) = \dim(N_{\text{FE,sel}})$ x $\dim(y)$, the *conditional network* applies 1D-convolutions (conv 1D) to process the data, which gradually increase in size to progressively extract higher-level features.

In general, the beam input would also be available in a 2D shape (property x spline nodes), though the feature selection of the sensitivity analysis reduced the splines irregularly. Thus, a 2D shape cannot be maintained anymore, as not all splines have the same number of nodes. Therefore, the selected beam input x for the updating process going into the cINN, is flattened to a vector and is not present in a 2D shape, as the beam response c is. However, as mentioned before, the conditions and input features are stacked in the *sub-networks* and thus need a similar spacial shape. Consequently, the *conditional network* has to flatten the shape to a vector for each output, in order to agree with the input shape in the sub-networks. Before flatting the output, the *conditional network* activates the convolutional layer output with a *parametric rectified linear unit* (PReLU) (He et al., 2015) and halves the dimension with an average 1D pooling layer (Chollet, 2018) (avg. pool 1D). After flattening, the dimension is additionally reduced with a fully connected layer (fc-layer) to subsequently relieve the sub-network's computation.

Within the cINN, the CCs are clustered into groups, which are then each fed by the progressively processed conditions c. All *sub-networks* have one hidden fc-layer, followed by a batch normalization to improve generalization and a PReLU (Chollet, 2018) activation layer, as depicted in Fig. 5. All hyperparameters of the complete network are summarised in Table 3.

The training is performed with an AdaGrad optimizer (Duchi et al., 2011) and an initial learning rate of 0.3, which is gradually decreased throughout the training process. The optimization minimizes the negative logarithmic likelihood (NLL) given in Eq. (3) in order to match the model's posterior prediction of $p_x(x|y)$ with the true posterior of the inverse problem (Noever-Castelos et al., 2021a).

$$\begin{aligned}\mathcal{L}_{\text{NLL}} &= \mathbb{E}\Big[-\log\big(p(x_i \mid y_i)\big)\Big] \\ &= \mathbb{E}\left[\frac{\|f(x_i;y_i)\|^2}{2} - \log|\det(J_i)|\right] + const. \end{aligned} \tag{3}$$

https://doi.org/10.5194/wes-2021-84
Preprint. Discussion started: 17 September 2021

Open Access
WIND ENERGY SCIENCE
DISCUSSIONS

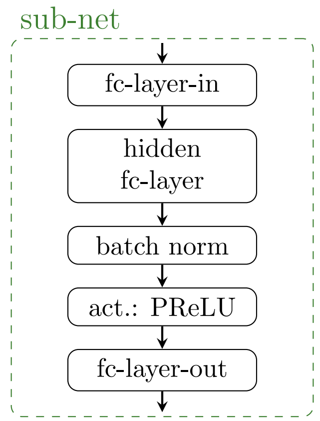

Figure 5. *Sub-network* with one hidden fully connected layer (fc-layer), batch normalization, and a PReLU activation layer. Each *conditional coupling blocks* CC has such a *sub-network* embedded.

Table 3. Hyperparameter set of the complete network, including *conditional network*, *conditional invertible neural networks* (cINN), and *sub-network*. The cINN is divided into 5 clusters, for which the hyperparameters are listed separately. In Cluster 1, the conditions are directly fed into the *conditional coupling blocks* CC, without a prior convolutional layer (cf. Fig. 4).

			Cluster 1	Cluster 2	Cluster 3	Cluster 4	Cluster 5
Conditional network	Conv 1D	kernel k		3	3	3	3
		stride s		1	1	1	1
		padding p		1	1	1	1
		out chan. out		32	64	128	256
	Activation			PReLU	PReLU	PReLU	PReLU
	Avgerage 1D pooling	kernel k		2	2	2	2
		stride s		2	2	2	2
		padding p		0	0	0	0
	Flatten		✓	✓	✓	✓	✓
	Fully connected	nodes	100	200	300	400	500
cINN	Conditional coupling block (CC)		3	3	3	3	3
Sub-network	Fully connected	nodes	400	500	600	700	800
	Batch normalization		✓	✓	✓	✓	✓
	Activation		PReLU	PReLU	PReLU	PReLU	PReLU

https://doi.org/10.5194/wes-2021-84
Preprint. Discussion started: 17 September 2021

4 Model Updating of a Rotor Blade Beam Model

Having selected the significant features with the sensitivity analysis and defined the cINN architecture, we will now move on to the model updating process and its evaluation. Therefore, the workflow of the cINN if briefly explained along with the schematic view of the transformations performed by the cINN in Fig. 6. The presented cINN in Sect. 3 is trained and tested with sample sets of input features x and their corresponding conditions c in the form of the modal beam responses as described in Sect. 2. During the training, the cINN is evaluated in the forward direction as depicted in Fig. 6, transforming the input features x into the normally distributed latent space z for given conditions c. The training is performed over 150 epochs, i.e., training iterations, with a samples size of 30,000 training samples, in order to minimize the $\mathcal{L}_{\mathrm{NLL}}$ (given in Eq. (3)). Additionally a sample set of 5,000 test samples, which have not been seen by the cINN during its training, are used for validating and testing the cINN after the training. All input features are always sampled randomly and independently, but at the same time, in order to span the complete parameter space. However, only features selected by the sensitivity study (cf. Table 2) are passed on to the cINN, as the other parameters are identified to be less relevant. As the cINN is trained to map the input features x into

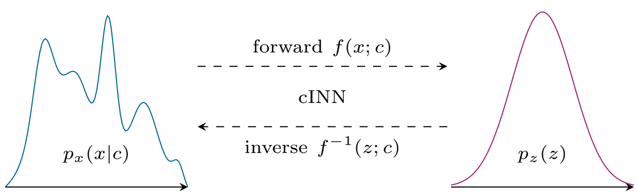

Figure 6. Schametic view of the transformation between the input features x and the latent space z for a given condition c performed by the conditional invertible neural network. (Noever-Castelos et al., 2021a)

a normally distributed latent space $p_z(z)$, during the inverse evalution the process is reversed: the latent space is sampled from a Gaussian normal distribution (e.g., 50-100 samples), which the cINN then transforms along with the beam response as condition c to the posterior prediction of the input features. This prediction results in a distribution for each input feature $p_x(x|y)$ as depicted in Fig. 6. In order to generalize the data for the training process and make it more comparable for the evaluation, all input features and conditions are standardized to zero mean and a standard deviation of 1 over the complete training set. The necessary scaling factors are additionally saved in the cINN to transform back and forth any input features or conditions used in the cINN besides the training process. Consequently, all features and conditions during the evaluation of the cINN are related to the complete training set's mean and standard deviation. Generally, the posterior predictions are also depicted with respect to their ground truth, i.e., target value of the sample, to align multiple samples for enhanced comparison.

This section first analyses the overall updating results of the model. The identified inference ambiguities are then highlighted and discussed, before the model is checked against its robustness to noisy conditions c_{noisy}. Based on the predicted posterior distribution of the input features $p(x|y)$, a resimulationn analysis is performed, where the updated parameters are used to feed the phyiscal model and calculate the beam response, in order to check the quality of the updating and sensitivity analysis results. Finally, a method for avoiding the computational intensive sensitivity analysis is presented.

https://doi.org/10.5194/wes-2021-84
Preprint. Discussion started: 17 September 2021

4.1 General Analysis of the Updating Results

In the first instance the posterior distributions have to be examined. Figure 7 shows as an example the predicted posterior distribution of four different input features as a histogram and fitted Gaussian distribution. The ground truth on the x-axis represents the real value used to generate the sample, while the distribution is obtained from the cINN. For the further analysis, the type of distribution must be known in advance for it to be possible to apply the correct metric, e.g., mean or median. In the case of a Gaussian distribution, the mean is the most significant value and will thus be applied in this study to reduce the posterior prediction distribution to a single value accompanied by the standard deviation as a measure of uncertainty.

By shifting the former x-axis from Fig. 7 onto the y-axis and reducing the distributions to their mean and standard deviation, as stated before, we obtain the graphs depicted in Fig. 8 for the same exemplary sample, but with all updated parameters. Most values range close to their ground truth value and with a narrow distribution, which is desired. For some input features, e.g., $\rho_{\mathrm{Biax90,N4}}$, the prediction is less accurate. However, the overall posterior prediction in this example is very good, as most of the values hit the ground truth.

After having checked the results in detail for one exemplary sample, Fig. 9 shows the prediction result of all selected input features for the 5,000 test samples. The feature description corresponding to each feature index can be looked up in Table 2. The graphs scatter the standardized mean posterior prediction $\bar{p}(x|y)$ against their corresponding target value from the sample set. Thus, the ideal case would correlate to an exact line with a slope $m = 1$. Each graph is equipped with the coefficient of determination R^2 and shows a corresponding regression line. Approximately 75% of the selected features reach a very satisfying linear correlation with $R^2 > 0.9$. Here, the authors would like to highlight that in the case of $\mathrm{feat}_{12,13,15}$ and $\mathrm{feat}_{21,22,24}$ the prediction losses in accuracy are due to intrinsic model ambiguities that will be discussed in the next section.

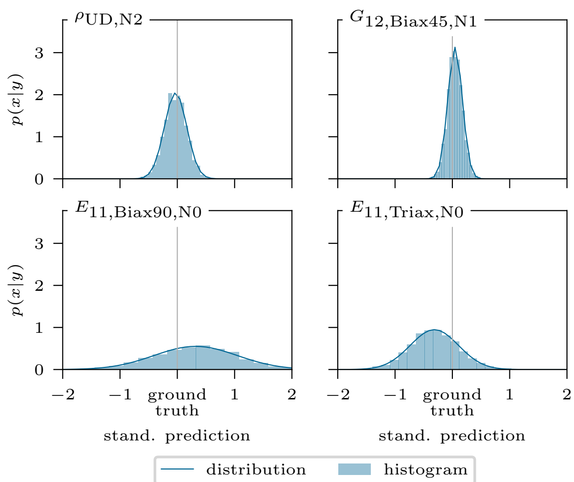

Figure 7. *Conditional invertible neural network's* standardized posterior prediction distributions $p(x|y)$ for four input features of one example. Plotted as a histogram and fitted Gaussian distribution.

https://doi.org/10.5194/wes-2021-84
Preprint. Discussion started: 17 September 2021

eawe european academy of wind energy
Open Access WIND ENERGY SCIENCE DISCUSSIONS

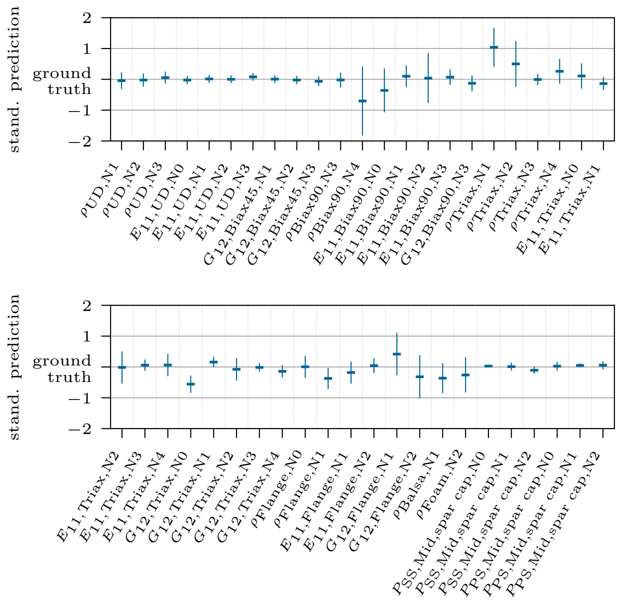

Figure 8. The first two graphs show the standardized posterior prediction for all updated input features related to the target value with 1-σ standard deviation as error, thus the mean value marks the distance to the target value, i.e., ground truth.

https://doi.org/10.5194/wes-2021-84
Preprint. Discussion started: 17 September 2021

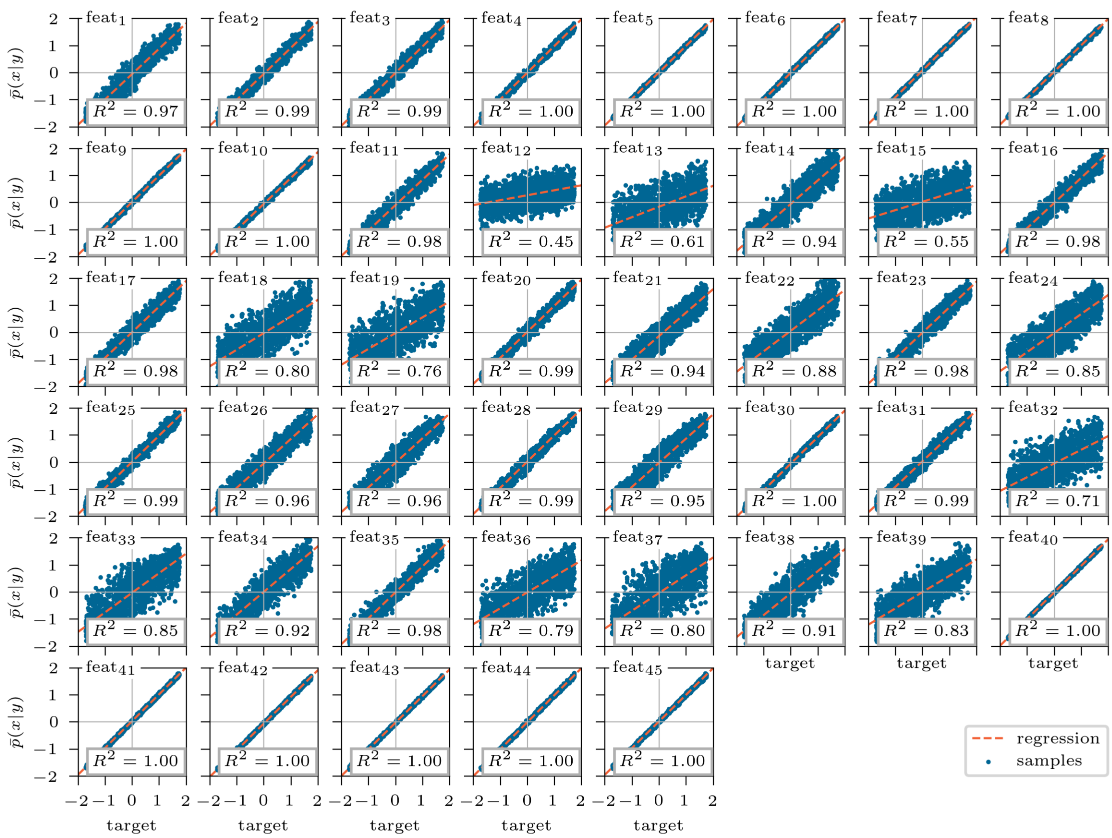

Figure 9. Standardized mean of posterior prediction $\bar{x}$ of the updated inputs over the corresponding target standardized value for the 5,000 test samples. The coefficient of determination and a corresponding linear regression line are shown. The corresponding parameter description to the features can be found in Table 2.

https://doi.org/10.5194/wes-2021-84
Preprint. Discussion started: 17 September 2021

4.2 Intrinsic Model Ambiguities

Ambiguities can originate from different sources, such as little significant responses or modeling issues (Ardizzone et al., 2019a). Noever-Castelos et al. (2021a) revealed some intrinsic model ambiguities of counteracting density values of the Biax90° and Triax layer in the blade cross-section. This was also handled by the cINN in this study, although it was only checked for the two spline nodes N_3 and N_4 (respectively feat$_{11,12}$ and feat$_{20,21}$), as these coincide in the feature selection. The results are depicted in Fig. 10, showing the standardized mean posterior prediction for the 5,000 test samples related to their ground truth and the linear regression as well as the corresponding slope m in the label. While the mean posterior predictions at node N_3 were detected rather accurately (cf. Fig. 8), i.e., represent a circular area in Fig. 10, the values of node N_4 spread more and correlate to the plotted regression line.

In addition to the density, another ambiguity was detected in the Young's modulus E_{11} of both these materials, shown in Fig. 11 for the nodes N_{0-3} (respectively feat$_{13-16}$ and feat$_{22-25}$). Here, the correlation of the mean posterior predictions is reasonably well described by the calculated regression lines. Finally, the last correlation was found for the shear modulus $G_{12,\text{N3}}$ (feat$_{17}$ and feat$_{30}$) between the same materials (Fig. 12).

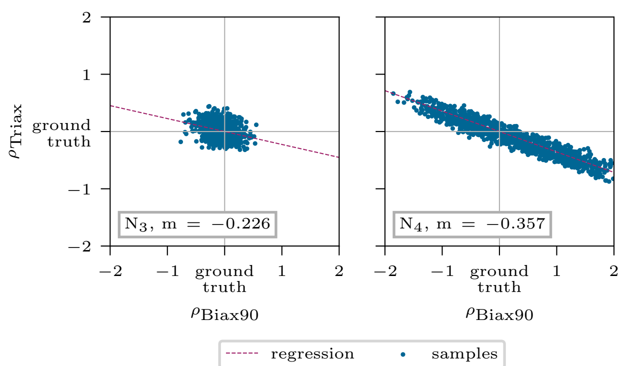

Figure 10. Interaction of density ρ_Biax90 and ρ_Triax describing the intrinsic model ambiguities. The depicted values correspond to the standardized mean posterior prediction for the 5,000 test samples.

All ambiguities rely on the same fact that the Biax90° and Triax layers appear subsequently in the stacking of the sandwich panels of the blade shell. The stacking is schematically illustrated in Fig. 13 with a detailed view of the shell, showing the stacking in exploded view. Together, these layers build the symmetric inner and outer face sheets of the shell, with a layer thickness of $t_\text{Biax90} = 0.651\,mm$ and $t_\text{Triax} = 0.922\,mm$, same density $\rho_\text{Biax90} = \rho_\text{Triax} = 1,875\,\frac{kg}{m^3}$, Young's modulus $E_{11,\text{Biax90}} = 26,430\,\frac{N}{mm^2}$ and $E_{11,\text{Triax}} = 29,873\,\frac{N}{mm^2}$, and shear modulus $G_{12,\text{Biax90}} = 3,464\,\frac{N}{mm^2}$ and $G_{12,\text{Triax}} = 6,918\,\frac{N}{mm^2}$.

https://doi.org/10.5194/wes-2021-84
Preprint. Discussion started: 17 September 2021

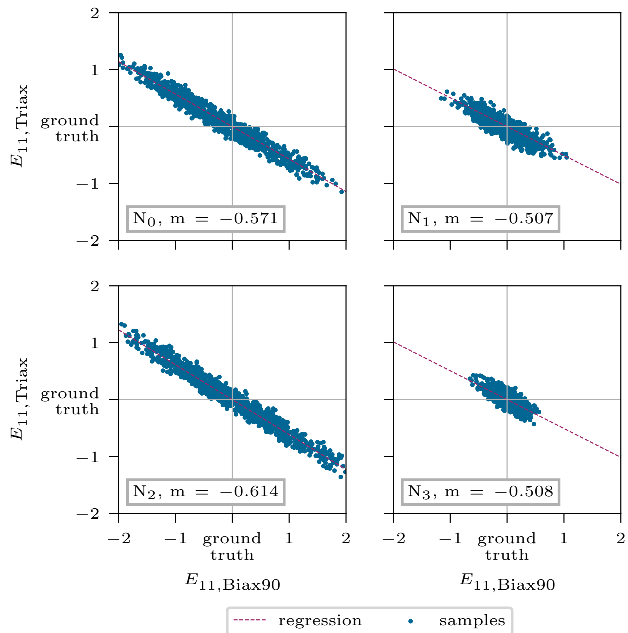

Figure 11. Interaction of stiffness $E_{11,\text{Biax90}}$ and $E_{11,\text{Triax}}$ describing the intrinsic model ambiguities. The depicted values correspond to the standardized mean posterior prediction for the 5,000 test samples.

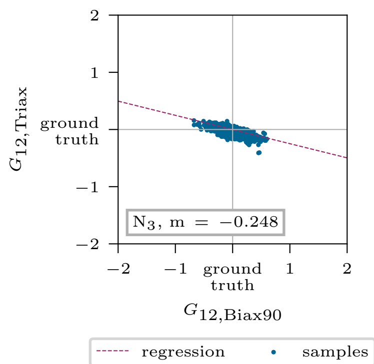

Figure 12. Interaction of shear stiffness $G_{12,\text{Biax90}}$ and $G_{12,\text{Triax}}$ describing the intrinsic model ambiguities. The depicted values correspond to the standardized mean posterior prediction for the 5,000 test samples.

The contributions of the properties to the model behavior must be analyzed for it to be possible to understand these ambiguities further. As described in Sect. 2, a finite element beam model is composed of beam elements containing cross-sectional properties (Blasques, 2012). These basically consist of mass and stiffness terms, which can be directly linked to ρ and E_{11} or G_{12}, respectively (Hodges, 2006). The upcoming deductions follow classical mechanics theories found for example in Gross

https://doi.org/10.5194/wes-2021-84
Preprint. Discussion started: 17 September 2021

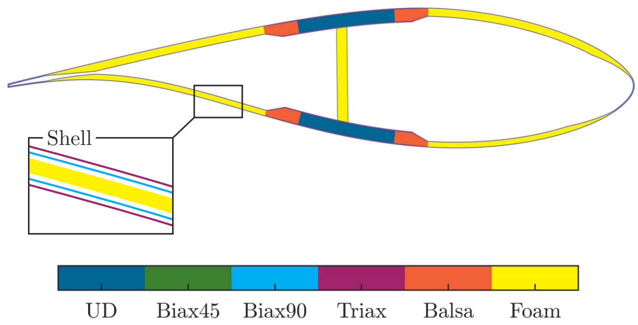

Figure 13. Schematic blade cross-sectional view at a radial position of $r = 12$ m with a detailed explosion drawing of the shell.

et al. (2012). First, considering the mass contribution, we stick with the simplified example of the center of gravity:

$$x_s = \frac{1}{m_{tot}} \int x^2 dm = \frac{1}{m_{tot}} \sum x_j^2 m_j \tag{4}$$

where x_j represents the center of gravity of each component and m_i the corresponding mass. Due to the very thin thickness of both layers and the overall cross-sectional dimension being about 10^3 greater for both materials, it can be assumed that $x_j = x_s$. And by expecting that the cINN correctly predicts the total mass m_{tot}, Eq. (4) yields:

$$x_s = \frac{1}{m_{tot}} \cdot x_s \sum m_j \tag{5}$$

$$m_{tot} = \sum m_j \tag{6}$$

$$= k_{\text{Biax90}} \cdot t_{\text{Biax90}} \cdot \rho_{\text{Biax90}} + k_{\text{Triax}} \cdot t_{\text{Triax}} \cdot \rho_{\text{Triax}} \tag{7}$$

And this obviously leads to the summation of all individual masses to the total mass, where k represents the number of layers. This of course holds for higher order moments of mass, due to the given proximity of both layers. Thus, a ratio between both materials can be expressed:

$$k_{\text{Biax90}} \cdot t_{\text{Biax90}} \cdot \rho_{\text{Biax90}} \; : \; k_{\text{Triax}} \cdot t_{\text{Triax}} \cdot \rho_{\text{Triax}} \tag{8}$$

A similar behavior is also found for the stiffness. This is explained in a simplified example for the flexural rigidity of a beam in Eq. (9), which extends with the Steiner theorem to Eq. (10).

$$EI_{\bar{x}} = \sum E_j I_{\bar{x},j} \tag{9}$$

$$= \sum E_j (I_{x,j} + x_s^2 \cdot A_j) \tag{10}$$

Assuming the layers have a rectangular shape, the area moment of inertia is $I_{x,j} = \frac{w \cdot t^3}{12}$, though the width w of the layer is large, the thickness t is 10^{-3} smaller and thus this term vanishes. With that, Eq. (10) reduces to Eq. (11). As stated before, x_s can be assumed to be constant and the same holds for the width w_i, as in the cross-sectional direction both material layers

https://doi.org/10.5194/wes-2021-84
Preprint. Discussion started: 17 September 2021

cover the complete circumference of the blade. This results in the proportionality in Eq. (12)

$$EI_{\bar{x}} = \sum E_j(x_s^2 \cdot A_j) = \sum E_j(x_s^2 \cdot k_j \cdot t_j \cdot w_j) \tag{11}$$

$$EI_{\bar{x}} \propto \sum E_j \cdot k_j \cdot t_j \tag{12}$$

Similarly, to the total mass m_{tot}, we expect the cINN to predict the global $EI_{\bar{x}}$ accurately and, consequently we can establish the following ratio for the stiffness:

$$k_{\text{Biax90}} \cdot t_{\text{Biax90}} \cdot E_{\text{Biax90}} \;:\; k_{\text{Triax}} \cdot t_{\text{Triax}} \cdot E_{\text{Triax}} \tag{13}$$

Analog derivations can be made for the shear modulus, which ends up in the ratio:

$$k_{\text{Biax90}} \cdot t_{\text{Biax90}} \cdot G_{\text{Biax90}} \;:\; k_{\text{Triax}} \cdot t_{\text{Triax}} \cdot G_{\text{Triax}} \tag{14}$$

Figure 14 shows the number of each layer for the respective material along the blade, which corresponds to both the inner and outer face sheet of the shell. The corresponding spline nodes positions are also depicted. Table 4 shows the ratios according to Eq. (8), Eq. (13), and Eq. (14) of the different possible stacking options in Fig. 14. Looking back to the identified ambiguities in

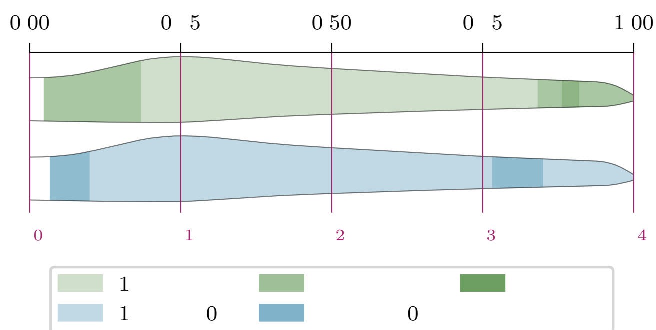

Figure 14. Layup of the sandwich laminate face sheets of the blade shell, consisting of Triax and Biax90°. The inner and outer face sheets are symmetric.

Table 4. Ratio between Biax90° and Triax layers for density and stiffness contribution, considering different layer constellation.

k_{Biax90}	1	1	1	2	2	2
k_{Triax}	1	2	3	1	2	3
$\frac{k_{\text{Biax90}} \cdot \rho_{\text{Biax90}} \cdot t_{\text{Biax90}}}{k_{\text{Triax}} \cdot \rho_{\text{Triax}} \cdot t_{\text{Triax}}}$	$\frac{0.706}{1}$	$\frac{0.353}{1}$	$\frac{0.235}{1}$	$\frac{1.412}{1}$	$\frac{0.706}{1}$	$\frac{0.471}{1}$
$\frac{k_{\text{Biax90}} \cdot E_{\text{Biax90}} \cdot t_{\text{Biax90}}}{k_{\text{Triax}} \cdot E_{\text{Triax}} \cdot t_{\text{Triax}}}$	$\frac{0.625}{1}$	$\frac{0.312}{1}$	$\frac{0.208}{1}$	$\frac{1.249}{1}$	$\frac{0.625}{1}$	$\frac{0.416}{1}$
$\frac{k_{\text{Biax90}} \cdot G_{\text{Biax90}} \cdot t_{\text{Biax90}}}{k_{\text{Triax}} \cdot G_{\text{Triax}} \cdot t_{\text{Triax}}}$	$\frac{0.354}{1}$	$\frac{0.177}{1}$	$\frac{0.118}{1}$	$\frac{0.707}{1}$	$\frac{0.354}{1}$	$\frac{0.236}{1}$

https://doi.org/10.5194/wes-2021-84
Preprint. Discussion started: 17 September 2021

Fig. 10 of the density at node N_4, the linear regression shows a slope of $m = -0.357$. Assuming each spline node contributes to the variance of half of the space to the left and right of it, the given slope agrees extremely well with the ratio of $k_{\text{Biax90}} = 1$ and $k_{\text{Triax}} = 2$. This corresponds to the stacking shown near the node N_4 in Fig. 14. Due to the poor linear regression of node N_3 in Fig. 10, the slope is not reliable, thus no conclusion can be drawn.

However, the counteracting Young's moduli in Fig. 11 can be very accurately captured by the ratios for most spline nodes. Starting with Node N_2 (figure 11 bottom-left), which is clearly affected by only one layer to the left and right of it (cf. Fig. 14), the line slope $m = -0.614$ matches the value in Table 4 ($k_{\text{Biax90}} = 1$, $k_{\text{Triax}} = 1$) of 0.625. Node N_0 has a slope of $m = -0.571$, which agrees well with the value corresponding to $k_{\text{Biax90}} = 2$ and $k_{\text{Triax}} = 2$, but tending towards $k_{\text{Biax90}} = 1$ and $k_{\text{Triax}} = 2$, which is also in the scope of this node according to the layup in Fig. 14. Similar behavior is found for node N_1. Node N_3 does not fully agree with this argumentation, though the point scatters less and the regression line might not be accurate enough. The same holds for the shear modulus in Fig. 12.

As assumed in the derivation of the ratios, we can state that the cINN should correctly predict the total mass and the stiffness contributions in a global manner, but suffers from an intrinsic model ambiguity affected by the counteracting densities ρ, Young's moduli E_{11}, and shear moduli G_{12} of the neighbouring materials Biax90° and Triax. However, it offers posterior predictions for these features, but with a wide distribution expressing the uncertainty of the cINN based on the given ambiguity. Merging both materials to a face sheet material following laminate theory, would avoid these ambiguities and improve the prediction qualities for the overall laminate. It is assumed that, based on the relatively low layer thickness, the infusion and therefore the fiber volume fraction of both layers is very similar, so that this approach should be valid.

4.3 Model Robustness

So far the analysis of this feasibility study was conducted on the exact test sample data, i.e., for a given input sample the corresponding exact output sample is generated with the tool chain MoCA + BECAS + ANSYS. In future studies, this presented method should be applied to real measured data of a blade and this normally suffers from measurement uncertainties. It is thus important to analyze the model robustness with respect to a measurement error of the output features. Therefore, an error of 5% as normally distributed random noise is applied to the clean output response of each sample, which is then used as a condition to infer the posterior prediction of the input features. The results are shown in Fig. A1 in the appendix, comparing the noisy (orange) and the clean (blue) mean posterior predictions $\bar{p}(x|y)$ against their corresponding targets for all 5,000 test samples. The graphs show some features that are sensitive for noise, such as feat$_4$ ($E_{11,\text{UD,N0}}$) or feat$_{34-37}$ ($E_{11,\text{Flange,N1-2}}$, $G_{12,\text{Flange,N1-2}}$), but most of the input features are predicted as accurate as with a clean output. Additionally,tests were performed resuming the training of the cINN with noisy conditions in order to improve the prediction quality, though no benefit was identified.

4.4 Resimulationn Analysis

A resimulationn analysis aims to utilize the posterior predictions of the cINN based on the original response to resimulate/recalculate the response with the physical model in order to compare it to the original response used to perform the prediction. For all samples, the correct input features and their corresponding response features are known, which we will be

https://doi.org/10.5194/wes-2021-84
Preprint. Discussion started: 17 September 2021

eawe european academy of wind energy
Open Access WIND ENERGY SCIENCE DISCUSSIONS

referring to as targets. The target response is used as a condition for the cINN to infer the posterior prediction of the selected input features. From these inferred input features we can create new input splines for each input, as depicted exemplarily in Fig. 15. However, the prediction is not a discrete value but a Gaussian distribution as we have seen before in Sect. 4.1. Additionally, there are nodes that the sensitivity analysis excluded from the updating process; these may take every value within their variation range, as they were sampled uniformly. Hence, for each input feature we obtain a range of possible splines as Fig. 15 illustrates. Here, the orange spline represents the target variance of the input parameter and the dark blue area represents the expected value, i.e., the mean prediction from the updated nodes. In the case of the first spline for ρ_{UD}, nodes N_0 and N_4 were excluded from the updating process and can thus take any value in the range of $\pm\,10\%$, as we do not have any prediction for them. As such the blue area covers all possible splines a user would take as the result from the model updating process. However, the purpose of this first evaluation of the resimulationn analysis is to examine, if sampling splines from the given distributions will all lead to appropriate results. Therefore, the $1-\sigma-$uncertainty displayed in light blue shows the standard deviation of the predicted nodes. In this first analysis, we sample uniformly from the not updated nodes (dark blue range) and normally distributed from the updated nodes (light blue) to create a spline. This will be done 1,000 times for the same given target response of the selected single test sample. Subsequently, these 1,000 sets of input splines are then used to create the model and calculate its modal response. For the sake of completeness, Table A2 gathers the identified mode shapes of both configurations. The resultant mode shapes of the free-free and the clamped configurations are then compared to the target response with the help of the modal assurance criterion (MAC) (Allemang, 2003).

$$\mathrm{MAC}_{ij} = \frac{|\Phi_i \cdot \Phi_j|^2}{|\Phi_i \cdot \Phi_i| \cdot |\Phi_j \cdot \Phi_j|} \tag{15}$$

The MAC is the scalar product of two normalized vectors, each representing all the model's degrees of freedoms of a particular mode shape. It is basically an orthogonality check: equal mode shapes reach a value of $\mathrm{MAC} = 1$, while a value of $\mathrm{MAC} > 0.8$ is already assumed to show good coherence (Pastor et al., 2012). For a multiple number of modes, a MAC matrix summarizes all MAC values of all mode shapes compared against each other.

In our use case, the MAC matrix is computed individually for all responses of the previously generated 1,000 samples against the target response. For the free-free configuration, Fig. 16 illustrates the mean value of the MAC matrix over all samples in the top graph. The corresponding standard deviation is depicted below. The main diagonal ideally takes values of $\mathrm{MAC}_{ij} = 1$, as the same mode shape of the sample and the target is compared. Additionally, the matrix should be symmetric, as the comparison of $\mathrm{MAC}_{ij} = \mathrm{MAC}_{ji}$ represents the same two mode shapes. Figure 16 confirms this ideal symmetric matrix structure for the re-simulated samples, with mean values $\overline{\mathrm{MAC}} > 0.9975$ in the diagonal and extremely low standard deviations of $\sigma_{\mathrm{MAC}} < 0.003$. For the clamped configuration, the values on the diagonal are also strikingly close to one ($\overline{\mathrm{MAC}} > 0.9960$, $\sigma_{\mathrm{MAC}} < 0.005$) and the overall matrix appears symmetric. In this way, sampling from the distribution predicted by the cINN for each selected input feature and arbitrarily choosing a value for the not updated values yields an exact coherence of target and computed mode shapes.

https://doi.org/10.5194/wes-2021-84
Preprint. Discussion started: 17 September 2021

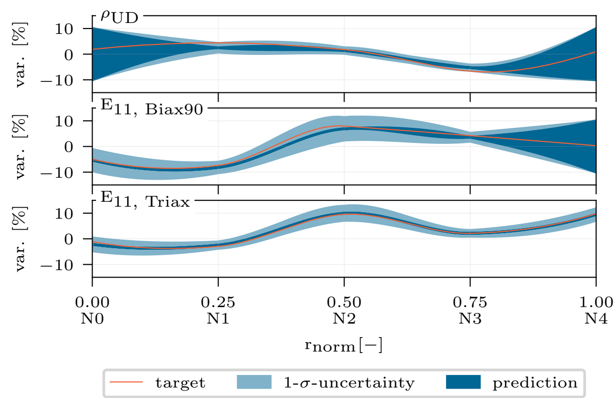

Figure 15. Exemplary inferred spline prediction range for ρ_{UD}, $E_{11,\mathrm{Biax90}}$ and $E_{11,\mathrm{Triax}}$. The graphs depict the target spline in orange, the mean prediction in dark blue, and the 1-σ-uncertainty in light blue, for the updated spline nodes.

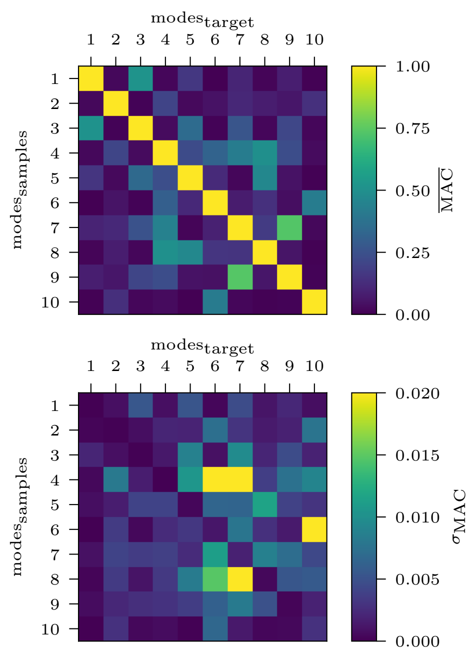

Figure 16. Mean values (top) and standard deviations (bottom) of the MAC matrix for the free-free modal configuration based on 1,000 spline samples inferred for one target response.

After having analysed a single target sample, the resimulationn is expanded to more samples to show the cINN's general performance. Therefore, posterior predictions for the 5,000 test samples of the test set are inferred with the cINN. Contrary to the resimulationn case before, only one input is generated for each of the samples by choosing the mean value of the prediction

https://doi.org/10.5194/wes-2021-84
Preprint. Discussion started: 17 September 2021

eawe european academy of wind energy
Open Access WIND ENERGY SCIENCE DISCUSSIONS

and, in the case of excluded variables, a node value of zero (i.e., no variation). That represents a typical choice a user would make, based on predicted posterior distributions. Figure 17 depicts the mean (horizontal marker), max and min value (bar) of the diagonal entries of the MAC matrices computed for all samples and both configurations, comparing the re-simulated model and their respective target response. Again, all mean values are extremely close to 1, so an overall excellent updating performance can be stated. Single predictions lead to worse results, as depicted by the minimum value, especially for the higher order modes, though the MAC value of less than 0.8 is only obtained for the 10th eigenmode of the free-free configuration.

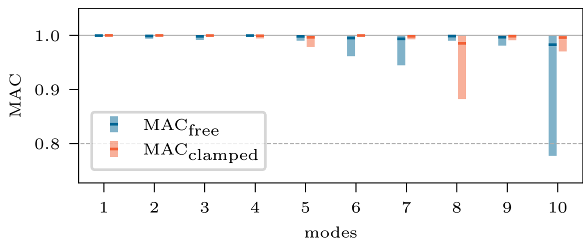

Figure 17. Mean, maximum, and minimum diagonal entries of the MAC matrices computed for 1,000 target responses.

The generally good performance is also confirmed by the predicted corresponding natural frequencies. Figure 18 shows the relative error from the re-simulated frequencies to the target frequencies of each mode for both configurations, giving the mean and standard deviation over all re-simulated samples. The range of the mean error is $|\bar{e}_f| < 0.25\%$ and the standard deviation $\sigma_{e_f} < 1.50\%$.

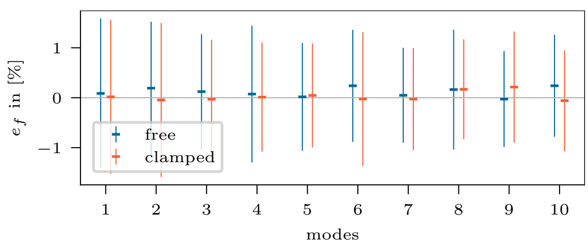

Figure 18. Mean and standard deviation of the natural frequency error e_f computed for 1,000 target responses.

The results of the presented resimulationn analysis show that:

1. The counteracting intrinsic model ambiguities cancel each other out, so the cINN correctly captures the global model behavior with respect to mass and stiffness distribution.
2. As expected, the insensitive and thereby excluded input parameters really do not have an impact on the results and can be chosen arbitrarily (cf. Fig. 15).
3. The overall cINN updating performance is strikingly good.

https://doi.org/10.5194/wes-2021-84
Preprint. Discussion started: 17 September 2021

4.5 Replacing Sensitivity Analysis

Similar to other model updating studies such as Luczak et al. (2014), this work relies on a sensitivity study to reduce the parameter space of the updating problem to significant parameters. This so-called feature selection, is performed in this particular investigation with the aforementioned Sobol method. A quasi-random sampling with low-discrepancy sequences (Dick and Pillichshammer, 2010) is applied to compute the Sobol indicies, which is a computational and space-efficient sampling method for the sensitivity analysis. However, the sampling set to train the cINN in general has to span a real random sampling space, where all features are varied independently, but simultaneously. That means, despite the 79,360 samples for the sensitivity analysis, an additional set of 30,000 samples has to be generated for training purposes and a second variably-sized set for validation and testing of the cINN. In total, this results in approximately 115,000 samples and thus model evaluations. This is crucial considering that the model evaluation in general is the computational bottleneck. Although a classical optimization algorithm would also need a feature selection to reduce the updating problem complexity on top of its usual model evaluation number for the optimization process, the overhead of the sensitivity cuts down the computational benefit of the cINN. A single model evaluation from creating the input parameter set to importing the modal response of the model took on average approx. 80 s on a single-core device. We generated the 115,000 samples on a 40-core computing cluster in slightly less than 2.66 days. In contrast, the cINN training for 150 epochs took only 0.67 h on an NVIDIA Tesla P100 GPU.

To reduce the computational sampling time, the idea is to apply the cINN on the full input parameter set x to identify relevant parameters. The cINN implicitly detects irrelevant features by predicting an uncertain posterior distribution, i.e., high standard deviation, due to missing information for the inference in the response. However, the current Sect. 4 and 4.2 showed that intrinsic model ambiguities lead to wider distributions, without being inaccurate in the global model behavior. This means the respective input parameters should not be rejected due only to a widely distributed posterior prediction. Therefore, we combine three metrics to perform the feature selection on the posterior predictions of the full input parameter set with respect to standardized values:

1. Root mean square error (RMSE) of the predicted posterior's mean and target value
2. Standard deviation of the predicted posterior distribution
3. Cross-correlation matrix of the predicted posterior's mean values

The RMSE should reject features that might have a narrow predicted posterior distribution, but do not match the target value. This is more a security or backup metric. The standard deviation is a metric for the confidence of the cINN and should reject features that are not significantly included in the information of the modal beam response. And finally, a cross-correlation matrix should reveal intrinsic model ambiguities from feature interactions, in order to keep the respective features, though the other two metrics would reject them. The cross correlation matrix of this inverse problem is depicted in Fig. 19. The input feat_{40-54} and feat_{60-74} in the matrix correspond to $\rho_{\text{Biax90,N0-N4}}$, $E_{11,\text{Biax90,N0-N4}}$, $G_{12,\text{Biax90,N0-N4}}$ and $\rho_{\text{Triax,N0-N4}}$, $E_{11,\text{Triax,N0-N4}}$, $G_{12,\text{Triax,N0-N4}}$, respectively, which show the high negative correlation of the interacting features discussed in Sect. 4.2. This matrix also helps to detect other relevant correlations. Especially nearby nodes of the same feature (e.g., features 85-87,

https://doi.org/10.5194/wes-2021-84
Preprint. Discussion started: 17 September 2021

WIND ENERGY SCIENCE DISCUSSIONS

$E_{11,\text{Flange,N0-2}}$) can counteract each other, as these have to predict in combination the spline behavior in between them, i.e., if one increases, the other has to diminish. Similar behavior was already detected in Bruns et al. (2019).

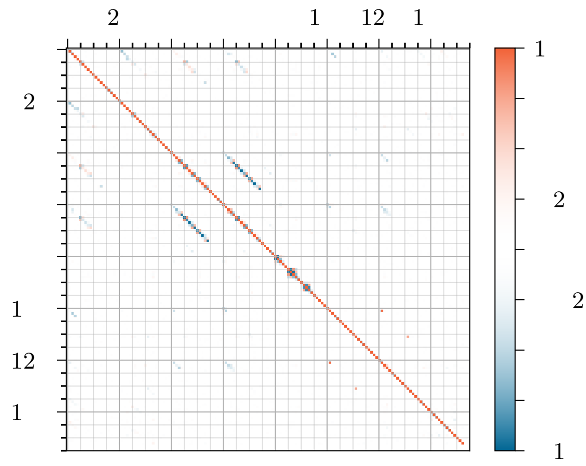

Figure 19. Cross-correlation of all input feature based on mean posterior prediction of the 5,000 test samples.

Similar to the Sobol threshold $S_{ij,thld} = 0.1$, thresholds for the given metrics can be chosen arbitrarily again and rely on experience. In this case we have chosen $\text{RMSE}_{thld} = 0.5$, $\sigma_{thld} = 0.5$, $\text{XCorr}_{thld,max} = -0.75$. Table A1 lists all features selected by the sensitivity analysis and the cINN in comparison. The sensitivity analysis selects 45 features, while the cINN includes 54 features. Most of the features agree for both selection methods, except those included in Table 5. The cINN, for example, includes the input features: $E_{11,\text{UD,N4}}$, $G_{12,\text{Biax45,N0}}$, $G_{12,\text{Balsa,N1}}$, which can be very well predicted by the cINN, but which are not detected by the sensitivity analysis to be significant for the response variations. Additionally, it detects a few highly negative correlating features: $E_{11,\text{Biax90,N4}}$ and $G_{12,\text{Biax90,N0-2,4}}$, which follow the similarly ambiguous behavior shown in the Sect. 4.2, counteracting the respective Triax properties. However, the features: $\rho_{\text{Triax,N1,2}}$, $\rho_{\text{Foam,N1}}$, detected by the sensitivity analysis were excluded by the cINN, though at least the first two show a significant $S_{max} > 0.200$.

Finally, this procedure is based on 30,000 samples and the same cINN architecture and hyperparameters. Figure A2 shows the correlation results for all features included in the sensitivity analysis, where the orange scatter represents the prediction with the model trained on the full input set and the blue scatter the prediction by the former model based on the feature selection from the sensitivity analysis. Only very few features show a significant loss in accuracy compared to the original model, and most likely for the feature with a worse prediction quality. Thus, there is no need to perform a second training process with a reduced data set for the sensitivity-free procedure, though the selection of the samples should still reveal the significant parameters of the model. Relying on the same computing resources mentioned above, the overall process in this particular case adds up to a complete computation time of approximately 20 h, which corresponds to a reduction of 69%. It also reveals that

https://doi.org/10.5194/wes-2021-84
Preprint. Discussion started: 17 September 2021

Table 5. Feature selection discrepancies between both methods: sensitivity analysis (SA) and the cINN-based approach, and their corresponding metrics.

Feature	SA	S_{max}	cINN	RMSE	σ	XCorr_{min}
$E_{11,\mathrm{UD,N4}}$		0.006	✓	0.340	0.354	-0.4407
$G_{12,\mathrm{Biax45,N0}}$		0.099	✓	0.196	0.156	-0.1787
$E_{11,\mathrm{Biax90,N4}}$		0.051	✓	0.913	0.881	-0.9524
$G_{12,\mathrm{Biax90,N0}}$		0.040	✓	0.862	0.833	-0.8341
$G_{12,\mathrm{Biax90,N1}}$		0.062	✓	0.454	0.374	-0.8889
$G_{12,\mathrm{Biax90,N2}}$		0.078	✓	0.941	0.920	-0.986
$G_{12,\mathrm{Biax90,N4}}$		0.009	✓	1.014	0.991	-0.9485
$\rho_{\mathrm{Triax,N1}}$	✓	0.292		0.648	0.531	-0.5367
$\rho_{\mathrm{Triax,N2}}$	✓	0.211		0.652	0.604	-0.6785
$E_{11,\mathrm{Flange,N0}}$		0.087	✓	0.713	0.597	-0.9262
$E_{11,\mathrm{Flange,N3}}$		0.044	✓	0.346	0.256	-0.6693
$G_{12,\mathrm{Flange,N3}}$		0.016	✓	0.405	0.410	-0.8762
$G_{\mathrm{Balse,N1}}$		0.017	✓	0.285	0.230	-0.2985
$\rho_{\mathrm{Foam,N2}}$	✓	0.163		0.623	0.538	-0.4732
$\rho_{\mathrm{Foam,N3}}$		0.072	✓	0.478	0.483	-0.5273

the cINN can handle a higher number of parameters, while extracting the relevant information from the response to predict the significant input features. On account of that, there is no need for a pre-analysing sensitivity study in future investigations.

5 Conclusions

The current study aims to extend the feasibility study of model updating with *invertible neural networks* presented in Noever-Castelos et al. (2021a) to a more complex and application-oriented level. The outstanding updating results presented in this study strengthens the conclusion in Noever-Castelos et al. (2021a) that *invertible neural networks* are highly capable to efficiently dealing even with an extensive wind turbine blade model updating.

In comparison with Noever-Castelos et al. (2021a), this investigation increased the model complexity from a single cross-sectional representation to a finite element beam model of the complete blade. The update parameter space was only slightly expanded for the materials to cover the most relevant, independent elastic properties of orthotropic materials. These, however, are varied over the complete blade length with 3 to 5 noded splines. Moreover, an established, global, variance-based sensitivity analysis with the Sobol method was performed to determine the relevant update parameters. A total of 45 input parameters were updated based on modal responses of the blade in a free-free boundary configuration and a root clamped configuration.

https://doi.org/10.5194/wes-2021-84
Preprint. Discussion started: 17 September 2021

The applied cINN approximately doubled its depth and an additional feedforward network was implemented to preprocess the conditions of the cINN in order to improve the network's flexibility and accuracy.

The result analysis of the predicted parameters shows strikingly high coherence with the target values with R^2 scores over 0.9 for 75% of the updated parameters. The very high updating certainty of the network is reflected in the narrow predicted posterior distributions of the updated parameters. Moreover, this study revealed more intrinsic model ambiguities of material properties (E_{11}, G_{12}, ρ) of the laminate face sheets Biax90° and Triax due to their proximity in the layup. The ambiguities are captured very accurately by the network. However, the resimulationn analysis revealed the modal response of the updated models matches the target results exceptionally well, with MAC values mostly above 0.97 and a mean error in the natural frequencies of $|\bar{e}_f| < 0.25\%$ over 1,000 randomly chosen test samples. Finally, this study presents a method for avoiding the computationally expensive sensitivity analysis by fully exploiting the opportunities of the cINN. For this reason, the full parameter set of $D_{tot} = 153$ was used for the update process. Thanks to the underlying probabilistic approach of the cINN, a similar set of significant input features was detected from the complete parameter space, based on the predicted posterior distributions and a cross correlation between the input feature to identify the ambiguities. Thus, the necessary sample number for the complete process was reduced to 30,000 samples and the computational time by 69%, while maintaining similar outstanding updating results.

In conclusion, the feasibility study was highly successfully extended to a full blade beam model, though with a still limited parameter set. The cINN proved to be extremely capable of performing an efficient model updating with a larger parameter space. Ongoing and future investigations should bring this method to a real life application. There, the parameter space will span more relevant aspects of blade manufacturing deviations, such as e.g., adhesive joints. Moreover, the combined laminate properties of the face sheets might be able to prevent the model ambiguities and even to improve the already good prediction accuracy.

Code and data availability. Code and data available in a publicly accessible repository:
https://github.com/IWES-LUH/Beam-ModelUpdating-cINN

https://doi.org/10.5194/wes-2021-84
Preprint. Discussion started: 17 September 2021

eawe european academy of wind energy
Open Access WIND ENERGY SCIENCE DISCUSSIONS

Appendix A: Tables & Figures

Table A1. Comparison of the feature selection performed by the sensitivity analysis (SA) and directly with the cINN applied to the full input parameter set.

Feature	SA	cINN	feature	SA	cINN
$\rho_{\text{UD,N1}}$	✓	✓	$E_{11,\text{Triax,N1}}$	✓	✓
$\rho_{\text{UD,N2}}$	✓	✓	$E_{11,\text{Triax,N2}}$	✓	✓
$\rho_{\text{UD,N3}}$	✓	✓	$E_{11,\text{Triax,N3}}$	✓	✓
$E_{11,\text{UD,N0}}$	✓	✓	$E_{11,\text{Triax,N4}}$	✓	✓
$E_{11,\text{UD,N1}}$	✓	✓	$G_{12,\text{Triax,N0}}$	✓	✓
$E_{11,\text{UD,N2}}$	✓	✓	$G_{12,\text{Triax,N1}}$	✓	✓
$E_{11,\text{UD,N3}}$	✓	✓	$G_{12,\text{Triax,N2}}$	✓	✓
$E_{11,\text{UD,N4}}$		✓	$G_{12,\text{Triax,N3}}$	✓	✓
$G_{12,\text{Biax45,N0}}$		✓	$G_{12,\text{Triax,N4}}$	✓	✓
$G_{12,\text{Biax45,N1}}$	✓	✓	$\rho_{\text{Flange,N0}}$	✓	✓
$G_{12,\text{Biax45,N2}}$	✓	✓	$\rho_{\text{Flange,N1}}$	✓	✓
$G_{12,\text{Biax45,N3}}$	✓	✓	$E_{11,\text{Flange,N0}}$		✓
$\rho_{\text{Biax90,N3}}$	✓	✓	$E_{11,\text{Flange,N1}}$	✓	✓
$\rho_{\text{Biax90,N4}}$	✓	✓	$E_{11,\text{Flange,N2}}$	✓	✓
$E_{11,\text{Biax90,N0}}$	✓	✓	$E_{11,\text{Flange,N3}}$		✓
$E_{11,\text{Biax90,N1}}$	✓	✓	$G_{12,\text{Flange,N1}}$	✓	✓
$E_{11,\text{Biax90,N2}}$	✓	✓	$G_{12,\text{Flange,N2}}$	✓	✓
$E_{11,\text{Biax90,N3}}$	✓	✓	$G_{12,\text{Flange,N3}}$		✓
$E_{11,\text{Biax90,N4}}$		✓	$\rho_{\text{Balsa,N1}}$	✓	✓
$G_{12,\text{Biax90,N0}}$		✓	$G_{\text{Balse,N1}}$		✓
$G_{12,\text{Biax90,N1}}$		✓	$\rho_{\text{Foam,N2}}$	✓	
$G_{12,\text{Biax90,N2}}$		✓	$\rho_{\text{Foam,N3}}$		✓
$G_{12,\text{Biax90,N3}}$	✓	✓	$P_{\text{SS,Mid,spar cap,N1}}$	✓	✓
$G_{12,\text{Biax90,N4}}$		✓	$P_{\text{SS,Mid,spar cap,N2}}$	✓	✓
$\rho_{\text{Triax,N1}}$	✓		$P_{\text{SS,Mid,spar cap,N3}}$	✓	✓
$\rho_{\text{Triax,N2}}$	✓		$P_{\text{PS,Mid,spar cap,N1}}$	✓	✓
$\rho_{\text{Triax,N3}}$	✓	✓	$P_{\text{PS,Mid,spar cap,N2}}$	✓	✓
$\rho_{\text{Triax,N4}}$	✓	✓	$P_{\text{PS,Mid,spar cap,N3}}$	✓	✓
$E_{11,\text{Triax,N0}}$	✓	✓			

https://doi.org/10.5194/wes-2021-84
Preprint. Discussion started: 17 September 2021

Table A2. Identified mode shapes of the first 10 modes (excluding rigid body motion) of the free-free and the clamped modal configuration.

Mode no.	Free-free	Clamped
1	1.Flap	1. Flap
2	1. Edge	1. Edge
3	2. Flap	2. Flap
4	1.Torsion	2. Edge
5	3. Flap	3. Flap
6	2. Edge	1. Torsion
7	4. Flap	4. Flap
8	2. Torsion	2. Torsion
9	5. Flap	3. Torsion
10	3. Edge	5. Flap

https://doi.org/10.5194/wes-2021-84
Preprint. Discussion started: 17 September 2021

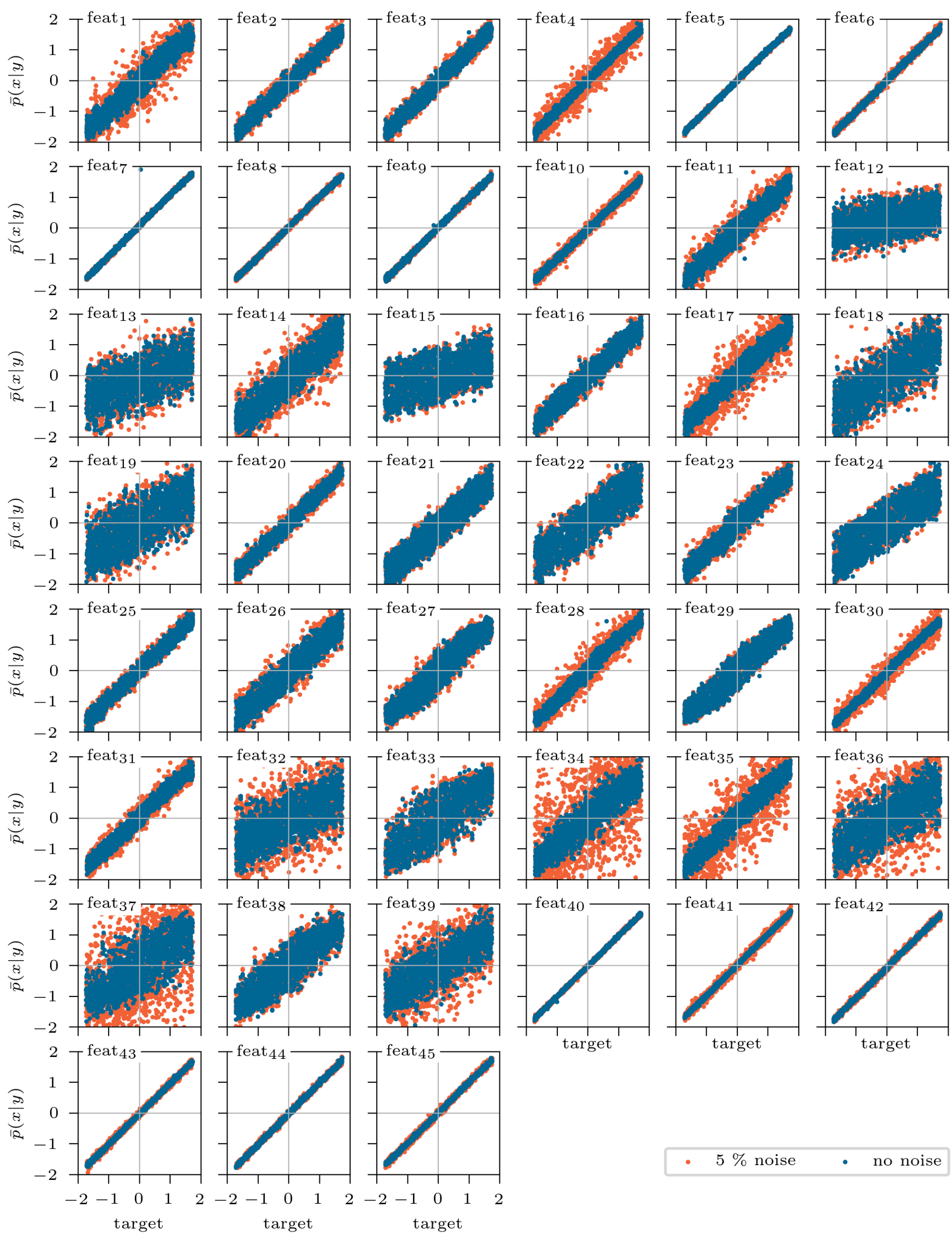

Figure A1. Standardized mean of posterior prediction $\bar{x}$ of the updated inputs over the corresponding target standardized value for the 5,000 test samples. The original samples predicted with clean conditions in blue, compared to samples with noisy flawed conditions (5% random noise) in orange. The noisy conditions are intended to simulate measurement inaccuracies of the modal beam response.

https://doi.org/10.5194/wes-2021-84
Preprint. Discussion started: 17 September 2021

WIND ENERGY SCIENCE DISCUSSIONS

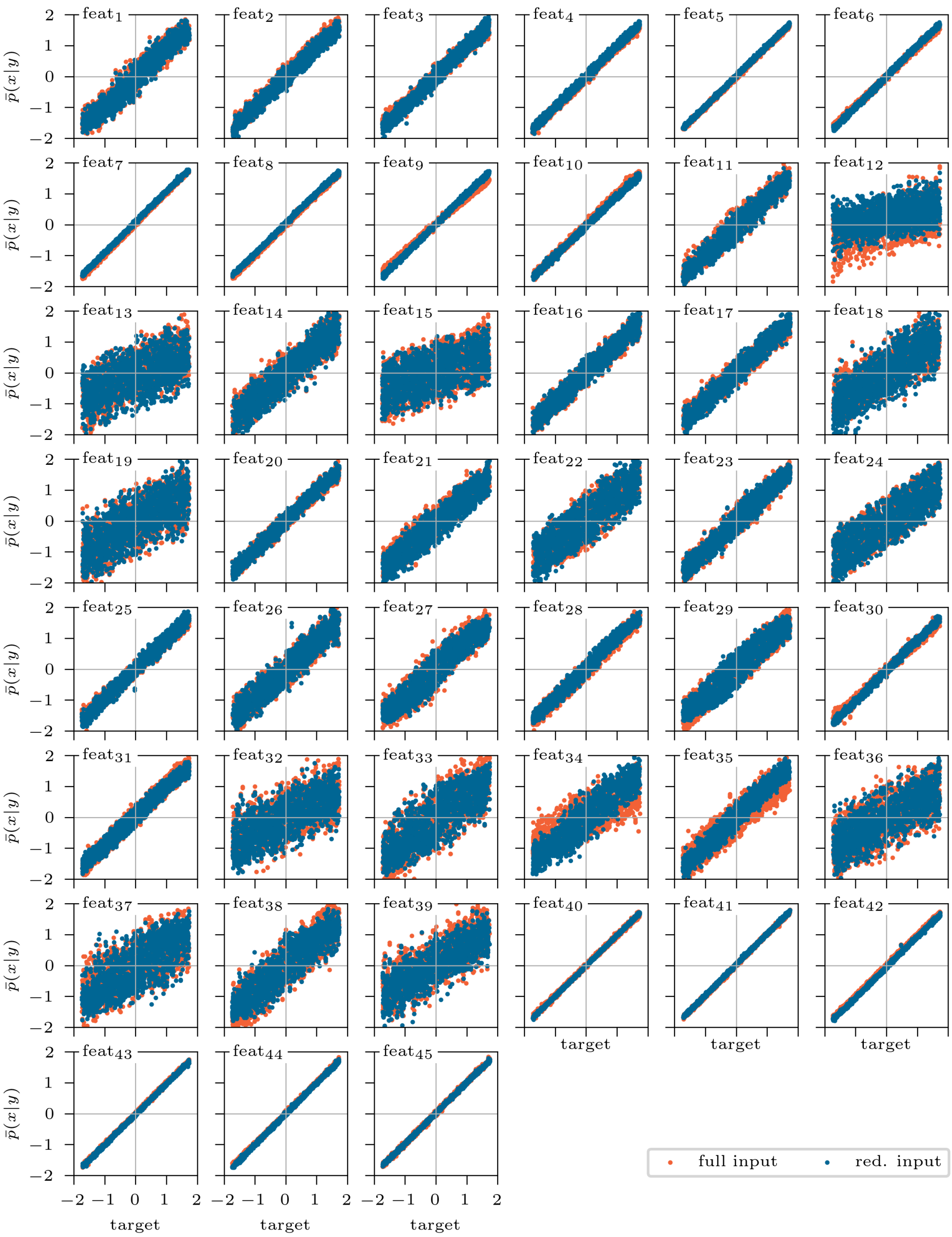

Figure A2. Standardized mean of posterior prediction $\bar{x}$ of the inputs selected by the sensitivity analysis, over the corresponding target standardized values for the 5,000 test samples. The original samples predicted with the reduced input set according to the sensitivity analysis selection are depicted in blue. They are compared with the inputs predicted by the cINN trained on the full input set (in orange).

https://doi.org/10.5194/wes-2021-84
Preprint. Discussion started: 17 September 2021

Author contributions. P.N-C.: conceptualization, methodology, software, validation, formal analysis, investigation, resources, data curation, writing–original draft preparation, writing–review and editing, visualization; D.M.: software, investigation, writing–review and editing; C.B.: writing–review and editing, supervision, project administration, funding acquisition. All authors have read and agreed to the published version of the manuscript.

Competing interests. The authors declare that they do not have any conflicts of interests.

Disclaimer. The information in this paper is provided as is and no guarantee or warranty is given that the information is fit for any particular purpose. The user thereof uses the information at its own risk and liability.

Acknowledgements. This work was supported by the Federal Ministry for Economic Affairs and Energy of Germany (BMWi) in the project ReliaBlade (grant numbers 0324335A/B).

This work was supported by the compute cluster, which is funded by the Leibniz University Hannover, the Lower Saxony Ministry of Science and Culture (MWK), and the German Research Association (DFG).

https://doi.org/10.5194/wes-2021-84
Preprint. Discussion started: 17 September 2021

References

Akima, H.: A New Method of Interpolation and Smooth Curve Fitting Based on Local Procedures, Journal of the ACM, 17, 589–602, https://doi.org/10.1145/321607.321609, 1970.

Allemang, R. J.: The modal assurance criterion - twenty years of use and abuse, Sound and Vibration, 37, 14–23, 2003.

ANSYS Inc.: Ansys® Academic Research Mechanical, Release 2021 R2, Help System, ANSYS Mechanical APDL Element Reference, 2021a.

ANSYS Inc.: Ansys® Academic Research Mechanical, Release 2021 R2, 2021b.

Ardizzone, L., Mackowiak, R., Rother, C., and Köthe, U.: Training Normalizing Flows with the Information Bottleneck for Competitive Generative Classification, in: 32nd Conference on Neural Information Processing Systems (NeurIPS 2018), vol. 33, pp. 7828–7840, 2018.

Ardizzone, L., Kruse, J., Wirkert, S., Rahner, D., Pellegrini, E. W., Klessen, R. S., Maier-Hein, L., Rother, C., and Köthe, U.: Analyzing Inverse Problems with Invertible Neural Networks, in: Seventh International Conference on Learning Representations, http://arxiv.org/pdf/1808.04730v3, 2019a.

Ardizzone, L., Lüth, C., Kruse, J., Rother, C., and Köthe, U.: Guided Image Generation with Conditional Invertible Neural Networks, http://arxiv.org/pdf/1907.02392v3, 2019b.

Augustyn, D., Smolka, U., Tygesen, U. T., Ulriksen, M. D., and Sørensen, J. D.: Data-driven model updating of an offshore wind jacket substructure, Applied Ocean Research, 104, 102 366, https://doi.org/10.1016/j.apor.2020.102366, 2020.

Blasques, J. P.: User's Manual for BECAS: A cross section analysis tool for anisotropic and inhomogeneous beam sections of arbitrary geometry, Denmark. Forskningscenter Risø, Risø DTU – National Laboratory for Sustainable Energy, 2012.

Blasques, J. P. and Stolpe, M.: Multi-material topology optimization of laminated composite beam cross sections, Composite Structures, 94, 3278–3289, https://doi.org/10.1016/j.compstruct.2012.05.002, 2012.

Bruns, M., Hofmeister, B., Pache, D., and Rolfes, R.: Finite Element Model Updating of a Wind Turbine Blade—A Comparative Study, in: EngOpt 2018 Proceedings of the 6th International Conference on Engineering Optimization, pp. 569–580, Springer International Publishing, Cham, https://doi.org/10.1007/978-3-319-97773-7, 2019.

Chollet, F.: Deep learning with Python, Safari Tech Books Online, Manning, Shelter Island, NY, http://proquest.safaribooksonline.com/9781617294433, 2018.

Chopard, B. and Tomassini, M., eds.: An Introduction to Metaheuristics for Optimization, Natural Computing Series, Springer International Publishing, Cham, https://doi.org/10.1007/978-3-319-93073-2, 2018.

Dick, J. and Pillichshammer, F.: Digital nets and sequences: Discrepancy theory and quasi-Monte Carlo integration, Cambridge Univ.Press, Cambrigde, 2010.

Duchi, J., Hazan, E., and Singer, Y.: Adaptive Subgradient Methods for Online Learning and Stochastic Optimization, Journal of Machine Learning Research, pp. 2121–2159, 2011.

Grieves, M. W.: Virtually Intelligent Product Systems: Digital and Physical Twins, in: Complex Systems Engineering: Theory and Practice, edited by Flumerfelt, S., Schwartz, K. G., Mavris, D., and Briceno, S., vol. 411, pp. 175–200, American Institute of Aeronautics and Astronautics, Inc, Reston, VA, https://doi.org/10.2514/5.9781624105654.0175.0200, 2019.

Gross, D., Hauger, W., Schröder, J., and Wall, W. A.: Technische Mechanik 2: Elastostatik, Springer-Lehrbuch, Springer, Berlin, 11., bearb. aufl. edn., 2012.

Gundlach, J. and Govers, Y.: Experimental modal analysis of aeroelastic tailored rotor blades in different boundary conditions, Journal of Physics: Conference Series, 1356, 012 023, https://doi.org/10.1088/1742-6596/1356/1/012023, 2019.

He, K., Zhang, X., Ren, S., and Sun, J.: Delving Deep into Rectifiers: Surpassing Human-Level Performance on ImageNet Classification, 2015.

Herman, J. and Usher, W.: SALib: An open-source Python library for Sensitivity Analysis, The Journal of Open Source Software, 2, 97, https://doi.org/10.21105/joss.00097, 2017.

Hodges, D. H.: Nonlinear composite beam theory, vol. 213 of *Progress in astronautics and aeronautics*, American Institute of Aeronautics and Astronautics, Reston, Va., 2006.

Hofmeister, B., Bruns, M., and Rolfes, R.: Finite element model updating using deterministic optimisation: A global pattern search approach, Engineering Structures, 195, 373–381, https://doi.org/10.1016/j.engstruct.2019.05.047, 2019.

Knebusch, J., Gundlach, J., and Govers, Y.: A systematic investigation of common gradient based model updating approaches applied to high-fidelity test-data of a wind turbine rotor blade, in: Proceedings of the XI International Conference on Structural Dynamics, pp. 2159–2174, EASDAthens, https://doi.org/10.47964/1120.9175.19508, 2020.

Lin, J., Leung, L. K., Xu, Y.-L., Zhan, S., and Zhu, S.: Field measurement, model updating, and response prediction of a large-scale straight-bladed vertical axis wind turbine structure, Measurement, 130, 57–70, https://doi.org/10.1016/j.measurement.2018.07.057, 2018.

Liu, X., Leimbach, K. R., and Hartmann, D.: System identification of a wind turbine using robust model updating strategy, in: Proceedings of 19th International Conference on the Application of Computer Science and Mathematics in Architecture and Civil Enrineering, pp. 250–260, Weimar, 2012.

Luczak, M., Manzato, S., Peeters, B., Branner, K., Berring, P., and Kahsin, M.: Updating Finite Element Model of a Wind Turbine Blade Section Using Experimental Modal Analysis Results, Shock and Vibration, 2014, 1–12, https://doi.org/10.1155/2014/684786, 2014.

Marwala, T., Boulkaibet, I., and Adhikari, S.: Probabilistic Finite Element Model Updating Using Bayesian Statistics, John Wiley & Sons, Ltd, Chichester, UK, https://doi.org/10.1002/9781119153023, 2016.

Noever-Castelos, P., Ardizzone, L., and Balzani, C.: Model updating of wind turbine blade cross sections with invertible neural networks, https://doi.org/10.15488/11045, 2021a.

Noever-Castelos, P., Haller, B., and Balzani, C.: Validation of a modelling methodology for wind turbine rotor blades based on a full scale blade test, https://doi.org/10.5194/wes-2021-24, 2021b.

Omenzetter, P. and Turnbull, H.: Comparison of two optimization algorithms for fuzzy finite element model updating for damage detection in a wind turbine blade, in: Nondestructive Characterization and Monitoring of Advanced Materials, Aerospace, Civil Infrastructure, and Transportation XII, edited by Shull, P. J., p. 60, SPIE, https://doi.org/10.1117/12.2295314, 2018.

Pastor, M., Binda, M., and Harčarik, T.: Modal Assurance Criterion, Procedia Engineering, 48, 543–548, https://doi.org/10.1016/j.proeng.2012.09.551, 2012.

Patelli, E., Govers, Y., Broggi, M., Gomes, H. M., Link, M., and Mottershead, J. E.: Sensitivity or Bayesian model updating: a comparison of techniques using the DLR AIRMOD test data, Archive of Applied Mechanics, 87, 905–925, https://doi.org/10.1007/s00419-017-1233-1, 2017.

Saltelli, A., Ratto, M., Andres, T., Campolongo, F., Cariboni, J., Gatelli, D., Saisana, M., and Tarantola, S.: Global Sensitivity Analysis: The Primer, John Wiley & Sons, New York, NY, 2008.

https://doi.org/10.5194/wes-2021-84
Preprint. Discussion started: 17 September 2021

Sayer, F., Antoniou, A., Goutianos, S., Gebauer, I., Branner, K., and Balzani, C.: ReliaBlade Project: A Material's Perspective towards the Digitalization of Wind Turbine Rotor Blades, IOP Conference Series: Materials Science and Engineering, 942, 012 006, https://doi.org/10.1088/1757-899X/942/1/012006, 2020.

Schröder, K., Grove, S., Tsiapoki, S., Gebhardt, C. G., and Rolfes, R.: Structural Change Identification at a Wind Turbine Blade using Model Updating, Journal of Physics: Conference Series, 1104, 012 030, https://doi.org/10.1088/1742-6596/1104/1/012030, 2018.

Sehgal, S. and Kumar, H.: Structural Dynamic Model Updating Techniques: A State of the Art Review, Archives of Computational Methods in Engineering, 23, 515–533, https://doi.org/10.1007/s11831-015-9150-3, 2016.

Sobol', I. M.: Sensitivity estimates for nonlinear mathematical models, Mathematical Modelling and Computational Experiment, 1, 407–414, 1993.

Sobol', I. M.: Global sensitivity indices for nonlinear mathematical models and their Monte Carlo estimates, Mathematics and Computers in Simulation, 55, 271–280, https://doi.org/10.1016/S0378-4754(00)00270-6, 2001.

Velazquez, A. and Swartz, R. A.: Operational model updating of low-order horizontal axis wind turbine models for structural health monitoring applications, Journal of Intelligent Material Systems and Structures, 26, 1739–1752, https://doi.org/10.1177/1045389X14563864, 2015.

Visual Learning Lab Heidelberg: FrEIA - Framework for Easily Invertible Architectures, https://github.com/VLL-HD/FrEIA, 2021.